Journal of Applied Fluid Mechanics, Vol. 18, No. 6, pp. 1446-1458, 2025.
Available online at www.jafmonline.net, ISSN 1735-3572, EISSN 1735-3645.
https://doi.org/10.47176/jafm.18.6.3249

A Study on a Semi-empirical Model for the Local Loss Coefficient of Small Angle Contraction Pipes

H. Sun, X. Zhu, X. Wang†, J. Zhao, S. Hu and J. Yu

State Key Laboratory of Fire Science, University of Science and Technology of China, Hefei 230026, China

†*Corresponding author email: wxs@ustc.edu.cn*

ABSTRACT

The design of contraction pipes for efficient fluid transport and spraying applications requires a deep understanding of fluid dynamics and resistance characteristics. This study utilizes the infinitesimal element method to analyze the fluid motion within the cross-section of a circular contraction pipe and confirms that the wall shear stress is a function of the total pressure gradient and pipe diameter, in accordance with Stokes' formula. Numerical simulations are employed to investigate the velocity distribution and transverse pressure loss pattern across the cross-section of the pipe. By making reasonable assumptions and conducting data fitting, we present a semi-empirical model that predicts pressure loss and local loss coefficients in small contraction pipes. This model is shown to be simpler, more accurate, and broadly applicable, compared with existing models. This study provides practical guidance for the design of contraction pipes and enhancement of the accuracy of pressure loss calculations, which are crucial for optimizing fluid transport systems.

Article History

Received November 11, 2024
Revised January 17, 2025
Accepted February 3, 2025
Available online March 30, 2025

Key words:

Contraction pipe
Stokes' formula
Numerical simulation
Pressure loss
Local loss coefficient

1. INTRODUCTION

As a primary method of fluid transmission, pipeline-conveying systems have garnered increasing interest in terms of performance optimization and energy conservation. The local loss coefficient is a crucial parameter representing the energy loss resulting from structural variations within the pipeline system, such as elbows, valves, and changes in the pipe diameter, while the fluid is in motion. The precise assessment of the local loss coefficient is important for optimizing pipeline design, enhancing fluid transfer efficiency, and curbing energy consumption (Liu et al., 2023; Wu et al., 2024).

The general expression for local loss, resembling Darcy's formula, can be represented as $h_m=\xi\frac{v^2}{2g}$, where ξ is a dimensionless quantity that represents the local loss coefficient and v typically denotes the average velocity of the inlet pipe (Daugherty et al., 1985). Local losses frequently occur in the structural components of pipelines, with the internal flow fields in these components being highly intricate, rendering the analysis of local losses challenging. In most cases, the local loss is determined experimentally. Nevertheless, theoretical analysis may be feasible for certain variable diameter pipelines under suitable assumptions.

Bae and Kim (2014a, b) conducted a numerical study on the turbulent flow in an axisymmetric sudden expansion with chamfered edges. They extensively explored the correlation between the local loss coefficient, Reynolds number, and main geometric parameters. They introduced a novel relationship for the local loss coefficient during a sudden expansion with chamfered edges. In Japan, Iguchi and Ohmi (1986) experimentally determined the local loss coefficient for sudden expansion and contraction pipelines and proposed an empirical relationship equation. Numerous scholars (Scott et al., 1986; Pak et al., 1990; Badekas & Knight, 1992; Shames, 1992; Oliveira et al., 1998; Yan & Gu, 2013) have conducted substantial research on the local loss coefficients of sudden expansion and contraction pipelines via experimental or simulation methods. Hence, they developed a wide array of effective models and empirical formulas (Eq. (1)) that are widely accepted and utilized in the field. In addition, Shames (1992) proposed another expression ($\xi_s=(\frac{d_c}{d_2}-1)$) of a sudden contraction pipe based on experimental results, where d_c represents the diameter of the vena contraction.

$$\xi_e=\left(1-\frac{d_1^2}{d_2^2}\right)^2 \quad \text{(for sudden expansion)}$$

or

$$\xi_s=0.42\left(1-\frac{d_1^2}{d_2^2}\right) \quad \text{(for sudden contractions)} \qquad (1)$$

Bullen et al. (1988) presented experimental data for

NOMENCLATURE

A_1	area of the smaller pipe	u'	horizontal pulsation velocity
A_2	area of the larger pipe	u_i	velocity of the micro element
C_1, $C_{1\varepsilon}$, C_2, G_b,σ_k, σ_ε	fluent parameters	v'	vertical pulsation velocity
d_1	diameter of the smaller pipe	V	average velocity in the pipe
d_2	diameter of the larger pipe	ΔP	static pressure difference between the two ends of the micro element
h_m	head loss	ΔP_t	total pressure difference between the contraction pipe
k_1	assumed coefficients between the dimensionless parameters $u/\bar{u}$ and y/r	Δr	radius difference between the two ends of the micro element
k_2	assumed coefficients between l and r	ΔS	area difference between the two ends of the micro element
l	Prandtl mixing length	Δx	thickness of the micro element in the x direction
P_s	static pressure in the pipe	**Greek symbols**	
P_{s0}	inlet static pressure in the pipe	α	angle of contraction and expansion of the pipe
P_{si}	micro element cross section static pressure in the pipe	τ	wall shear stress
P_t	total pressure in the pipe	τ_v	viscous shear stress
P_{t0}	inlet total pressure in the pipe	τ_t	Reynolds stress
R	inlet radius of the contraction pipe	μ	coefficient of air viscosity
Re	Reynolds number of the fluid in the pipe	ρ	air density
S_0	inlet area of the pipe	ξ	local loss coefficient
S_x	outlet area of the pipe	ξ_{max}	local loss coefficient (divided by the larger pipe dynamic pressure)
u_0	inlet velocity of the contraction pipe	ξ_{min}	local loss coefficient (divided by the smaller pipe dynamic pressure)
$\bar{u}$	average velocity		

the variation of the pressure loss coefficient with inlet sharpness and compared it with the approximate data, showing significant differences at higher sharpness values. Hooper (1981, 1988) proposed numerous empirical formulas for pipe dimensional changes, such as sudden contraction and expansion as well as gradual contraction and expansion. They obtained these formulas by dividing the asymptotic microdivision into individual microelementary sudden contraction pipes and then integrating the loss coefficient of the gradual contraction, as shown in Eq. (2). However, the local loss coefficient obtained using this method only correlates with the contraction angle, which is an imperfect representation. The local loss coefficient also depends on the geometric parameters (Gosteev et al., 2018) (which can be expressed as the ratio of the diameters on both sides of the reducer to the contraction angle).

$$\xi = \begin{cases} 1.6\sin\left(\dfrac{\alpha}{2}\right) & (0°<\alpha<45°) \\ \sqrt{\sin\left(\dfrac{\alpha}{2}\right)} & (45°<\alpha<180°) \end{cases} \tag{2}$$

A widely employed expression for the local loss coefficient of a contraction pipe is given by Eq. (3) (Rennels, 2022). The equation illustrates a positive correlation between the local loss coefficient of the contraction pipe and Darcy friction factor when the pipeline operates under standard conditions. It also elucidates the connection between the local loss coefficient and pipeline size.

$$\xi = \frac{\lambda}{8\sin\alpha}\left(1-\left(\frac{A_1}{A_2}\right)^2\right) \tag{3}$$

However, calculating the Darcy friction factor, particularly for turbulent flows, requires the use of empirical formulas (Yogaraja et al., 2021) or Moody's charts (Daugherty et al., 1985; Brown, 2002), which can introduce significant errors.

In terms of measurement techniques, instruments such as rotational viscometers and rheometers (Abou-Kassem et al., 2023) are used for stress analysis, whereas pressure sensors (Xu et al., 2024) and pitot tubes are used

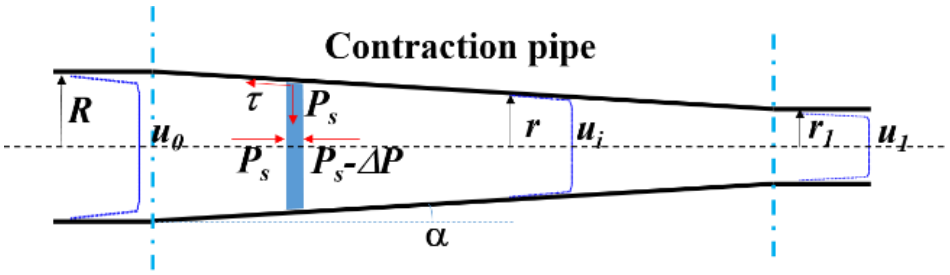

Fig. 1 Model of a circular gradual contraction pipe

to measure the pipe pressure. However, a nonuniform velocity distribution within pipes can lead to an uneven pressure distribution, revealing the limitations of these methods.

Ayas et al. (2021) introduced an approximate method based on the Metzner and Reed theory (1955) to estimate the loss coefficients of noncircular ducts with an error margin of less than 5%, compared with traditional methods. Sobieski (2024) employed numerical simulation approaches via the *k–ω* shear stress transport (SST) turbulence model to investigate pressure losses in pipes of various cross-sections, and they derived an empirical relationship between the loss coefficient and Reynolds number, demonstrating high accuracy and reliability. Yao et al. (2019) utilized the building block approach to calculate the pressure losses in contraction–expansion pipes, achieving a relative error within 15%.

In summary, the numerical simulation method has a certain degree of reliability. Thus, this study focuses on gradual contraction pipes and aims to establish a local loss model by combining theoretical analyses with numerical simulations to address the need for a more efficient, convenient, and highly accurate local loss coefficient.

2. THEORETICAL MODEL

The simplified model of the circular axisymmetric contracting pipe flow shown in Fig. 1 makes several key assumptions to facilitate the analysis. These assumptions are crucial for simplifying the problem and deriving meaningful insights regarding fluid flow behavior. Each assumption is explained as follows.

1) Incompressible Fluid: The assumption of an incompressible fluid implies that the fluid density remains constant throughout the flow field. This assumption simplifies the mathematical description of the flow by eliminating the need to consider changes in density with respect to time, which is expressed as $d\rho/dt=0$.

2) Constant Flow: This assumption implies that flow properties, such as pressure, velocity, and density, at any given point in the fluid do not change with time. That is, the flow is assumed to be in a steady state with no time-dependent fluctuations in the flow field. This assumption simplifies the governing equations and allows for a time-independent analysis of the flow behavior.

3) Neglecting Gravity: By ignoring the effects of gravity, the model assumes that gravitational forces have a negligible impact on the flow behavior being studied.

4) Smooth and No-slip Boundary Conditions: The assumption that the pipe wall is smooth implies that there are no rough elements that could affect the flow. Additionally, the assumption of a no-slip boundary condition implies that the fluid in direct contact with the pipe wall has the same velocity as the wall itself.

These assumptions collectively facilitate the setup of a simplified model for analyzing circular axisymmetric contracting pipe flows and thus enable the derivation of theoretical solutions that provide insights into flow behavior under idealized conditions.

Consider a small section of the contraction pipe, as shown in Fig. 1, as a microelement body. The force analysis was primarily affected by the positive fluid stress on the two end faces, positive and shear stresses on the control body wall surface, and average static pressure everywhere. If the average static pressure on the left side of the control body is P_s, the right side is (P_s-ΔP), the wall surface is P_s, and the wall shear stress is τ, then the motion equation of the control body can be derived.

$$\mathrm{P}_s\pi r^2-(\mathrm{P}_s-\Delta\mathrm{P})\pi(r-\Delta r)^2-\tau\Delta\mathrm{S}\times\cos(\alpha)-\mathrm{P}_s\Delta\mathrm{S}\times\sin(\alpha)=\rho\Delta\mathrm{V}u_i\frac{\partial u}{\partial x} \tag{4}$$

The wall contact area of this control body is ΔS, as shown in Eq. (5).

$$\Delta\mathrm{S}=\frac{1}{2}\frac{r}{\sin\alpha}\times2\pi r-\frac{1}{2}\frac{r\text{-}\Delta r}{\sin\alpha}\times2\pi(r-\Delta r)=\frac{2\pi r}{\sin\alpha}\times\Delta r \tag{5}$$

Then, Eq. (4) can be simplified to give:

$$\Delta\mathrm{P}\pi r^2-2\pi r\tau\Delta x=\rho\Delta\mathrm{V}u_i\frac{\partial u}{\partial x} \tag{6}$$

The control body volume ΔV can be expressed as ($\Delta V=\pi r^2\Delta x$) and ($\Delta r=\Delta x\cdot tan\alpha$). As the fluid was incompressible, the flow rates in each section were equal.

$$u_0\pi\mathrm{R}^2=u_i\pi\mathrm{r}^2$$

$$u_i=\frac{u_0\mathrm{R}^2}{r^2}=\frac{u_0\mathrm{R}^2}{(\mathrm{R}-x\tan\alpha)^2} \tag{7}$$

Therefore, we can obtain:

$$u\frac{\partial u}{\partial x}=\frac{2u_0^2\mathrm{R}^4\tan\alpha}{(\mathrm{R}-x\tan\alpha)^5} \tag{8}$$

The final simplification gives:

$$\frac{\Delta \mathrm{P}}{\Delta x}=-\frac{dP_s}{dx}=\frac{2\tau}{\mathrm{R}-x\tan\alpha}+\frac{2\rho u_0^2\mathrm{R}^4\tan\alpha}{\left(\mathrm{R}-x\tan\alpha\right)^5} \tag{9}$$

According to Bernoulli's equation:

$$\mathrm{P}_{s0}+\frac{1}{2}\rho u_0^2=\mathrm{P}_{si}+\frac{1}{2}\rho u_i^2+\Delta \mathrm{P}_t \tag{10}$$

Here ΔP_t denotes the full pressure loss. Therefore, the expression of the average static pressure of the cross-section P_s can be obtained as follows:

$$\mathrm{P}_{si}=\mathrm{P}_{s0}+\frac{1}{2}\rho u_0^2\left(1-\frac{\mathrm{R}^4}{r^4}\right)-\Delta \mathrm{P}_t \tag{11}$$

Differentiating by x yields:

$$\frac{d\mathrm{P}_s}{dx}=\frac{dP_t}{dx}-\frac{2\rho u_0^2\mathrm{R}^4\tan\alpha}{\left(\mathrm{R}-x\tan\alpha\right)^5} \tag{12}$$

Combining Eq. (9) with Eq. (12), we obtain:

$$\frac{dP_t}{dx}=-\frac{2\tau}{\mathrm{R}-x\tan\alpha}=-\frac{2\tau}{r} \tag{13}$$

Alternatively:

$$\tau=-\frac{r}{2}\frac{dP_t}{dx} \tag{14}$$

These results indicate that the fluid wall shear stress in the contraction pipe satisfies Stokes' formula (Daugherty et al., 1985):

$$\tau=\frac{Gr}{2} \tag{15}$$

However, G in Eq. (15) is not constant and represents the total pressure gradient.

$$\mathrm{G}=\frac{\Delta \mathrm{P}_t}{\Delta x}=-\frac{dP_t}{dx} \tag{16}$$

This theoretical derivation and the following numerical simulation are validated against each other.

3. NUMERICAL SIMULATION

3.1 Modeling and Mesh Independence Analysis

Fluent is a computational fluid dynamics (CFD) software package that is used worldwide and allows for the simulation of complex flows encompassing both incompressible and highly compressible regimes. Fluent offers various physical models to address diverse physical problems (Yan et al., 2012). In this study, Ansys Fluent 2019R3 was employed to perform numerical simulations.

The initial stage involves the construction of a three-dimensional pipe model, as depicted in Fig. 2(a). The pipe model featured an inlet diameter of 0.63 m and length of 3 m for the contraction section. Moreover, both before and after the contraction section, the model featured a rectification section measuring 1 m in length. This model

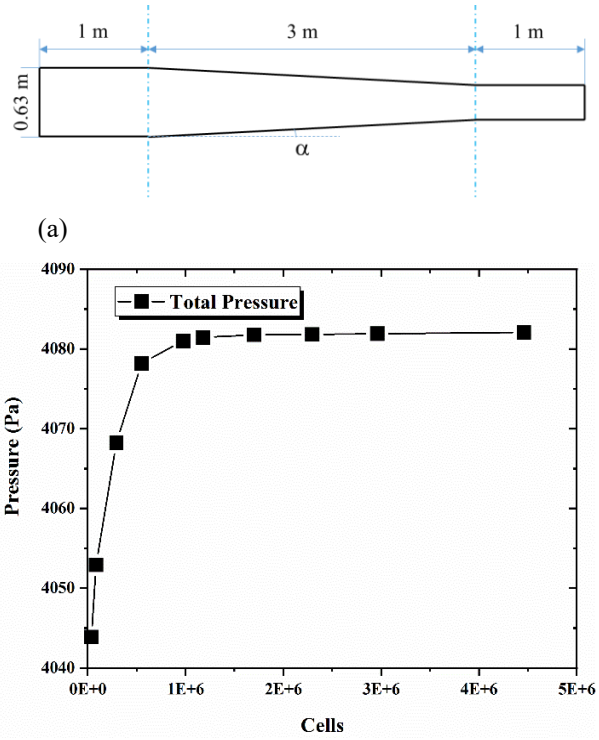

Fig. 2 (a) Front view of the 3D model constructed in the simulation. (b) Mean pressure of the cross-section at x=1 m for the grid independence test

is a simplified version of a turbofan fire cannon manufactured by a company. Parallelepiped mesh rendering was selected for a more accurate pipe flow simulation.

To ensure that the numerical results were not artifacts of grid resolution, a mesh independence study was conducted for the contraction pipe flow case with a 3° contraction angle (denoted by α) and an inlet velocity of 20 m/s. We assessed the impact of varying the grid size on the simulation results by focusing on the total pressure at the pipe outlet as a primary metric.

The study involved a series of simulations with grid sizes ranging from 7 to 40 mm, with each having a different number of grid cells. The results indicated that when the grid size was finer than 11 mm (the number of cells exceeded one million), the outlet pressure showed negligible variation (Fig. 2(b)), suggesting that the flow field was well-resolved at this grid density. To ensure a conservative and accurate simulation, we selected a grid size of 10 mm for our numerical simulations to provide robust grid resolution while maintaining computational efficiency. This choice of grid size allows for a reliable representation of the flow dynamics within the contraction pipe, as evidenced by a mesh independence study.

Furthermore, we calculated the required first boundary layer grid thickness for the case in which y^+ was between 30 and 300. The calculation indicated that the first layer grid thickness ($\Delta y=\frac{y^+}{u^*}$) should be between 0.63 and 6.3 mm. Consequently, we added five layers of boundary layer grids with an expansion ratio of 1.2 near the walls. The grid thickness of the first layer was calculated to be approximately 1.552 mm, which is

sufficient to satisfy the precision requirements.

3.2 Simulation Settings

In Fluent, the pressure-based solver was utilized, the *k–ε* realizable turbulence model (Shih et al., 1995; FLUENT User's Guide, 2019; Liu et al., 2021) was chosen for the flow model, and the standard wall function was applied. The transport equations for turbulent kinetic energy and its dissipation rate in this model are provided below.

$$\rho\frac{\mathrm{D}k}{\mathrm{D}t}=\frac{\partial}{\partial x_j}\left[\left(\mu+\frac{\mu_t}{\sigma_k}\right)\frac{\partial k}{\partial x_j}\right]+\mathrm{G}_k+\mathrm{G}_b-\rho\varepsilon-\mathrm{Y}_\mathrm{M}$$

$$\rho\frac{\mathrm{D}\varepsilon}{\mathrm{D}t}=\frac{\partial}{\partial x_j}\left[\left(\mu+\frac{\mu_t}{\sigma_\varepsilon}\right)\frac{\partial \varepsilon}{\partial x_j}\right]+\rho\mathrm{C_i S}\varepsilon-\rho\mathrm{C}_2\frac{\varepsilon^2}{\mathrm{k}+\sqrt{\upsilon\varepsilon}}+\mathrm{C}_{1\varepsilon}\frac{\varepsilon}{\mathrm{k}}\mathrm{C}_{3\varepsilon}\mathrm{C_b} \tag{17}$$

In the given context, $C_1=\max\left[0.43,\frac{\eta}{\eta+5}\right]$, $\eta=\frac{Sk}{\varepsilon}$, G_k represents the turbulent energy generation term resulting from the mean velocity gradient, G_b signifies the turbulent energy generation term derived from buoyancy, and Y_M denotes the impact of compressible turbulent pulsation expansion on the total dissipation rate. Constants $C_{1\varepsilon}$ and C_2 are defined, and σ_k and σ_ε represent the turbulent Prandtl numbers for the turbulent kinetic energy and dissipation rate, respectively. In Fluent, the values are set as follows (Launder & Spalding, 1972; Wilcox, 1994): $C_{1\varepsilon}$=1.44, C_2=1.9, σ_k=1.0, and σ_ε=1.2.

The boundary conditions were meticulously defined to ensure the accuracy and reliability of the simulation results. The inlet velocity was calculated based on a summary of the turbulent velocity distribution inside a pipe by Štigler (2014), and the expression was formulated as 20.0375 [m·s^-1]·(1-((sqrt(*x*·*x*+*y***y*))/0.315 [m^1])^1066). The inlet had a hydraulic diameter of 630 mm. The outlet was specified as a pressure outlet with a gauge pressure of 0 Pa and set against an ambient pressure of 101,325 Pa, representing standard atmospheric conditions. All walls were modeled as fixed, no-slip boundaries to accurately represent the fluid–structure interactions.

In this study, the ambient pressure at the exit was chosen as the boundary condition to simplify the analysis of the flow within the contraction pipe. This approach is prevalent in the literature (Sobieski, 2024) and allows for a clear examination of the impact of contraction on flow. The constraints of other boundary conditions may introduce additional variables that complicate the interpretation of the influence of contraction on the flow. Although we acknowledge that this condition may not reflect all realistic scenarios, it provides a controlled environment for studying the primary effects of contraction.

The SIMPLE method was employed owing to its effectiveness in solving the incompressible flow equations. A time step of 0.0001 s was selected to ensure numerical stability, per the CFL condition, which is crucial for the transient simulation of the flow within a contraction pipe. The total simulation time was set to 0.5 s, corresponding to 5000 time steps, based on a convergence study that indicated that this duration was sufficient for the flow to reach a statistically steady state.

To ascertain the attainment of a steady state, we monitored the key flow variables and their residuals. The flow was considered to have reached a steady state when these variables exhibited minimal variation between consecutive time steps and the residuals converged toward zero. A grid independence study was conducted to ensure that the chosen grid size was appropriate for capturing flow features without excessive computational costs.

4. ANALYSIS OF THE RESULTS

4.1 Contraction Pipe (α= 3°, u_0=20 m/s)

Based on the transient simulation results for an inlet velocity of 20 m/s and a contraction angle of 3° (Fig. 3), several observations can be made. The velocity magnitude contours display a symmetrical and periodic flow pattern within the contraction section, indicating stable and repeatable flow behavior. The static pressure contours display a gradual pressure decrease along the contraction section, which is indicative of turbulent pressure loss and wall shear stress under the no-slip condition at the wall. Our study specifically addresses these losses, which are

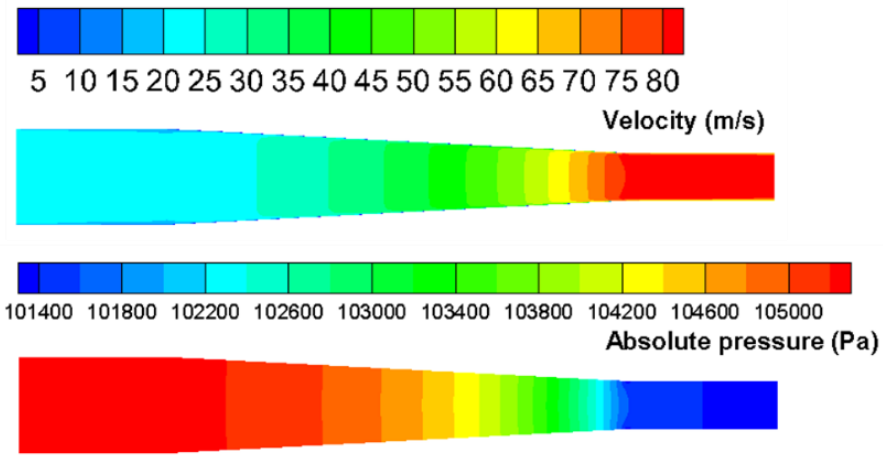

Fig. 3 Velocity and static pressure contours of the contraction pipe with an inlet velocity of 20 m/s and a contraction angle of 3°

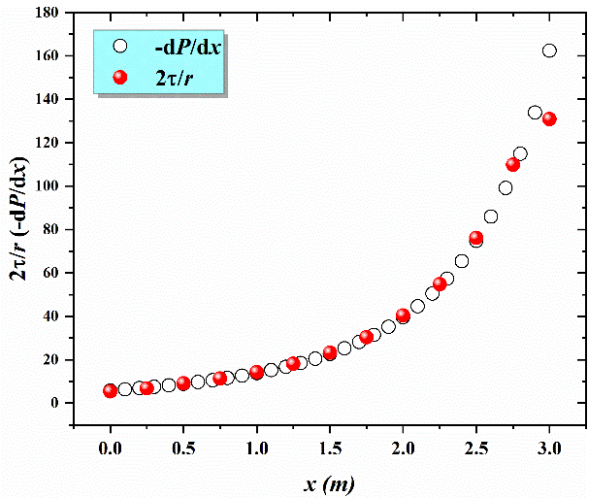

Fig. 4 Scatterplot of contraction pipe 2τ/r (-dP/dx) with respect to x

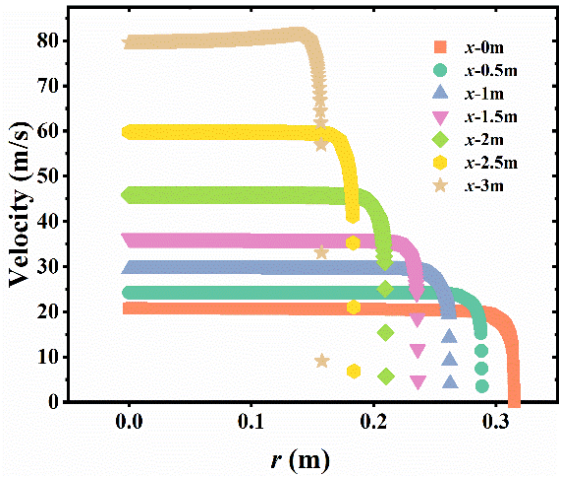

(a) Cross-sectional velocity distribution at different locations of the contraction pipe

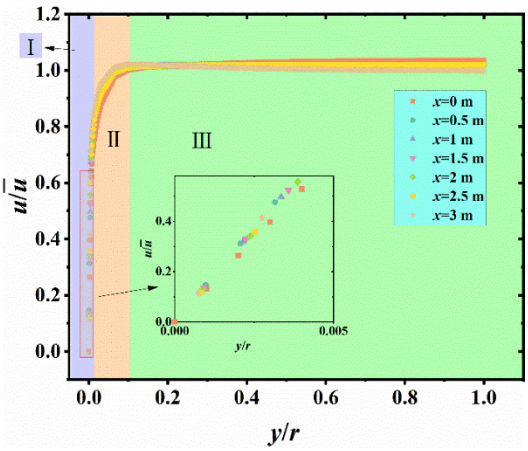

(b) Dimensionless velocity distribution of the cross-section at different locations of the contraction pipe

Fig. 5 Velocity distribution of the cross-section at different locations of a contraction pipe with an inlet velocity of 20 m/s and a contraction angle of 3°

critical to understanding the performance of contraction pipes under turbulent flow conditions.

Other potential pressure losses, such as those owing to vortex shedding, compressibility effects, and secondary flow effects, could occur under different flow conditions but were not included in our model. These phenomena are beyond the scope of this study and are centered on the internal flow behavior within the contraction section.

In conclusion, the results indicate that the designed contraction section functioned effectively under the specified conditions, displaying a stable flow pattern with pressure losses predominantly caused by turbulence and wall shear stress. Although other factors could have contributed to the pressure losses in more complex scenarios, they were not considered in this study.

The cross-sectional profiles were generated at various points along the contraction pipe. The total pressure in each section was recorded and differentiated, and the wall shear stress was measured. A plot comparing (-dP/dx) against (2τ/r) was constructed. As illustrated in Fig. 4, strong agreement between (-dP/dx) and (2τ/r) was observed, indicating the suitability of Stokes' formula.

Figure 5(a) illustrates the velocity distribution across the contraction pipe section at an angle of 3 °with an initial velocity of 20 m/s, which is consistent with Kao et al. (2017)'s results. The near-wall velocity was made dimensionless using Nikolas (1933)'s method for a fully turbulent smooth pipe flow. The y-axis represents the cross-sectional velocity u divided by the average cross-sectional velocity $\bar{u}$ *(y=u /$\bar{u}$)*, and the x-axis denotes the distance from the wall y divided by the section radius r *(x=y/r)*. The dimensionless velocity plots for each section exhibited significant consistency, allowing for delineation into three zones (Fig. 5(b)).

In zone I, the velocity gradient (viscous sublayer) adheres to Eq. (18), where k_1 is the hypothesis coefficient:

$$\frac{u}{\bar{u}} = k_1 \times \frac{y}{r} \tag{18}$$

Zone II is a transition zone in which velocity increases as a certain function.

Zone III is a core zone in which velocity either stabilizes or exhibits slow growth.

The shear stress in the x-direction consists of the viscous shear stress determined by the velocity gradient of the time-averaged velocity u in the y-direction and the turbulent pulsation shear stress (i.e., Reynolds stress) determined by the pulsation velocity.

$$\tau = \tau_v + \tau_t = \mu \frac{du}{dy} + \left(-\rho \overline{u'v'}\right) \tag{19}$$

In theory, near the wall, the velocity gradient is higher, and turbulent fluctuations are less pronounced, indicating that viscous shear stress should prevail, whereas Reynolds stress plays a secondary role. However, for an inlet velocity of 20 m/s and a contraction angle of 3 °, Fig. 5 (b) shows that the velocity gradient near the wall can be described by Eq. (20), where k_1 is a dimensionless coefficient.

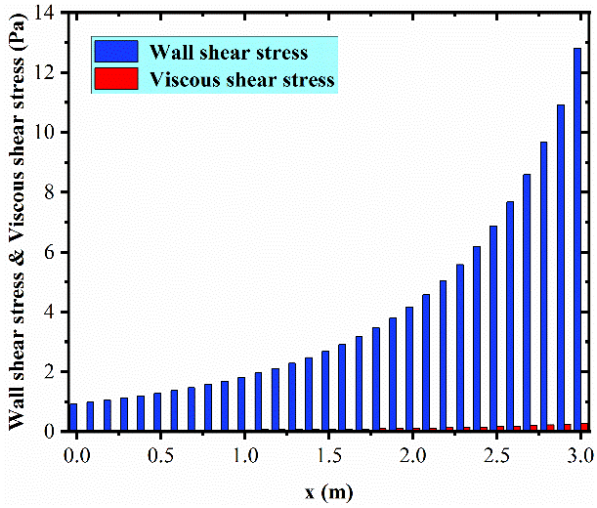

Fig. 6 Comparison of the magnitudes of the shear stress and viscous shear stress on the wall of the contraction pipe with an inlet velocity of 20 m/s and a contraction angle of 3°

$$\frac{\partial u}{\partial y}=\frac{k_1\bar{u}}{r}=\frac{k_1u_0\mathrm{R}^2}{r^3} \tag{20}$$

Therefore, the viscous shear stress was obtained as:

$$\tau_v=\frac{\mu k_1u_0\mathrm{R}^2}{r^3} \tag{21}$$

A linear fit of the dimensionless velocity near the wall in Fig. 5 (b) yields the following expression:

$$\frac{u}{\bar{u}}=29.66262\times\frac{y}{r} \tag{22}$$

Figure 6 shows a histogram displaying the wall shear stress and viscous shear stress near the wall of the contraction pipe. The total wall shear stress at the contraction pipe wall significantly surpasses the viscous shear stress component, which contributes less than 4% of the total, indicating that the wall turbulent pulsation shear stress dominates in the contraction pipe.

The *k*–*ε* realizable turbulence model provides a detailed and precise simulation of the flow field, which serves as a benchmark for the accuracy of our analytical predictions. Concurrently, we applied Prandtl's mixing length theory to estimate the Reynolds stress. The purpose of discussing both methods is to provide a comprehensive view of the problem in which the CFD simulations set a standard for accuracy and the analytical model offers a practical and simplified alternative for use in quick assessments.

The Prandtl mixing length theory relates the pulsation velocity either in the direction of the flow or vertically to the gradient of the time-averaged velocity via the introduction of a distance l at each point. The pulsation at a point can be expressed as ($u'\sim l\frac{\partial u}{\partial y}$). According to the continuity equation for incompressible fluids, the vertical pulsation velocity v' caused by the horizontal velocity u' possesses an equal magnitude but opposite sign to u', which can be represented as ($v'\sim -l\frac{\partial u}{\partial y}$). Therefore, the Reynolds stress can be formulated as follows (Daugherty et al., 1985):

$$\tau_t=-\rho\overline{u'v'}=\rho l^2\left(\frac{\partial u}{\partial y}\right)^2 \tag{23}$$

Prandtl assumed $l=k\cdot y$ based on experimental observations and a magnitude analysis. However, in this case, Prandtl's assumption regarding the mixing length l does not apply because the Reynolds stress at the wall remains dominant. Reflecting on the simulation data, it is valuable to initially assume that $l=k_2\cdot r$, which enables the calculation of the Reynolds stress (Eq. (24)) via combination with Eq. (22).

$$\tau_t=\frac{\rho k_1^2k_2^2u_0^2\mathrm{R}^4}{r^4} \tag{24}$$

Neglecting the viscous shear stress, the wall shear stress was approximately equal to the Reynolds stress, which thereby allowed the wall shear stress to be expressed as $\tau\propto\frac{1}{r^4}$. Using an inlet velocity of 20 m/s and a contraction angle of 3° for the contraction pipe as an example, the wall shear stress was plotted as a function of r, as shown in Fig. 7.

Figure 7(a) displays the alignment of the wall shear stress with $y=A\times x^{-4}$ (coefficient of determination: $\mathrm{R}^2=0.99813$) and the reliability of the assumed mixing length $l=k_2\cdot r$.

To further analyze the pressure loss coefficient of the contraction pipe, the average total pressure of the cross-section of the contraction pipe was studied, leading to the derivation of Eq. (25) via the combination of Eqs. (13) and (24):

$$\frac{d\mathrm{P}_t}{dx}=-\frac{2\tau}{r}=-\frac{2\rho k_1^2k_2^2u_0^2\mathrm{R}^4}{r^5}=-\frac{2\rho k_1^2k_2^2u_0^2\mathrm{R}^4}{(\mathrm{R}-x\tan\alpha)^5}=-\frac{2\rho k_1^2k_2^2u_0^2\mathrm{R}^4\tan\alpha^{-5}}{(\mathrm{R}/\tan\alpha-x)^5} \tag{25}$$

The average total pressure of each section along the axis of the contraction pipe was initially determined and differentiated in the x-direction to obtain $\frac{d\mathrm{P}_t}{dx}$. Figure 7(b) illustrates the total pressure gradient and corresponding fitted curve. The graph demonstrates that the total pressure loss gradient satisfies the criterion $\frac{d\mathrm{P}_t}{dx}\propto\frac{1}{r^5}$, and the coefficient of determination ($\mathrm{R}^2=0.99892$) indicates excellent agreement, further confirming the reliability of the assumption of $l=k_2\cdot r$.

The total pressure expression was obtained by integrating Eq. (25):

$$\mathrm{P}_t=\int\frac{d\mathrm{P}_t}{dx}=\int-\frac{2\rho k_1^2k_2^2u_0^2\mathrm{R}^4\tan\alpha^{-5}}{(\mathrm{R}/\tan\alpha-x)^5}=\mathrm{C}-\frac{\rho u_0^2k_1^2k_2^2\mathrm{R}^4}{2\tan\alpha(\mathrm{R}-x\tan\alpha)^4} \tag{26}$$

Therefore, the total pressure loss (Eq. (27)) can be expressed as the total pressure difference between the inlet

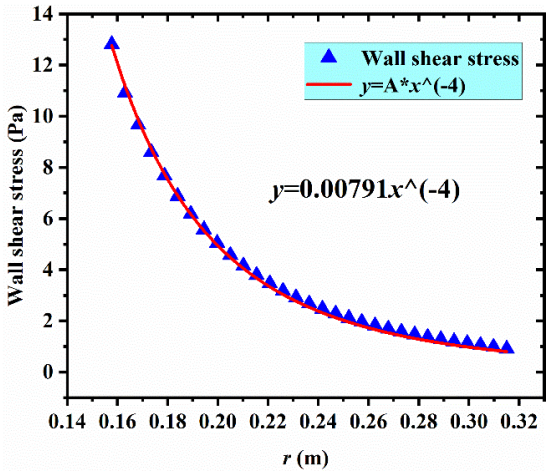

(a)

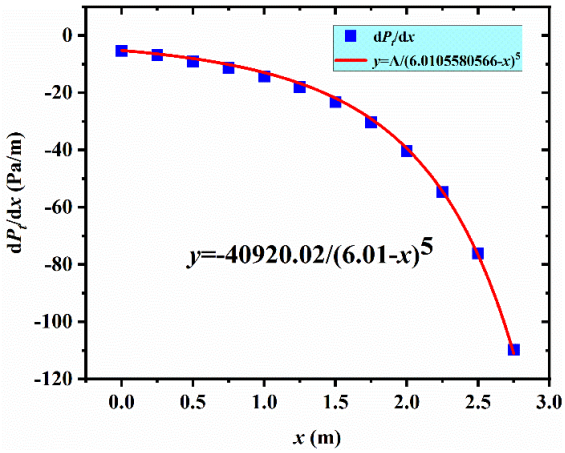

(b)

Fig. 7 (a) Variation of shear stress at the wall with radius *r* of the contraction pipe with an inlet velocity of 20 m/s and a contraction angle of 3°. (b) Gradient of total pressure loss along the *x*-direction of the contraction pipe with an inlet velocity of 20 m/s and a contraction angle of 3°

and outlet of a contraction pipe:

$$\Delta P_t\big|_0^x = P_{t0} - P_{tx} = \frac{\rho u_0^2 k_1^2 k_2^2}{2\tan\alpha}\left(\frac{R^4}{(R - x\tan\alpha)^4} - 1\right) = \frac{\rho u_0^2 k_1^2 k_2^2 \left(R^4 - r^4\right)}{2\tan\alpha r^4} \tag{27}$$

Based on the general expression of local loss following the Cauchy formula (Brown, 2002) ($\Delta P = \xi \cdot \frac{1}{2}\rho u^2$), the contraction pipe pressure loss coefficient can be expressed as given in Eq. (28). Here, ξ_{max} was obtained by dividing the dynamic pressure of the large pipe, whereas ξ_{min} was obtained by dividing the dynamic pressure of the small pipe.

$$\xi_{max} = \frac{\Delta P_t}{\frac{1}{2}\rho u_0^2} = \frac{k_1^2 k_2^2}{\tan\alpha}\left(\frac{R^4}{r^4} - 1\right) = \frac{k_1^2 k_2^2}{\tan\alpha}\left(\frac{S_0^2}{S_x^2} - 1\right)$$

$$\xi_{min} = \frac{\Delta P_t}{\frac{1}{2}\rho u_x^2} = \frac{k_1^2 k_2^2}{\tan\alpha}\left(1 - \frac{r^4}{R^4}\right) = \frac{k_1^2 k_2^2}{\tan\alpha}\left(1 - \frac{S_x^2}{S_0^2}\right) \tag{28}$$

Equation (28) is similar to Eq. (3) in that it demonstrates the specific relationship between the local loss coefficient of the contraction pipe and pipe structure. Next, it is necessary to discuss the specific influential parameters k_1 and k_2.

4.2 Relationships Between k_1, k_2, and Inlet Velocity (*Re*)

The method of controlling variables was employed to analyze the effect of the inlet Reynolds number on k_1 and k_2. Specifically, the process involved maintaining a constant pipe contraction structure (with a fixed contraction angle of 3° and constant length of 3 m) and adjusting the Reynolds number by varying the inlet velocity. Table 1 lists 10 different operating conditions with varying Reynolds numbers.

Based on previous research, two critical aspects must be analyzed: obtaining the linear distribution of the velocity near the wall and the gradient of the axial total pressure variation under each condition. These factors enable the determination of specific k_1 and k_2 values at different inlet velocities.

Figure 8 illustrates the specific value of k_1 in the linear distribution expression of the viscous sublayer velocity for different initial inlet velocities obtained via linear fitting (only four sets of typical values are presented). However, the specific value of k_2 was indirectly obtained based on the fitted relational equation for the axial full pressure gradient. Figure 9 depicts the variations in k_1 and k_2 at different inlet velocities, indicating that k_1 is independent of the initial velocity, whereas k_2 decreases with larger initial velocities within the studied range. Because k_2 is dimensionless and can be physically interpreted as the distance traveled by a fluid microcluster before dissipation, it is closely linked to the Reynolds number. These results motivated the direct exploration of their relationships. Figure 9 demonstrates that k_2 sharply decreases as Re decreases for Re < 100000, whereas k_2 slowly decreases as Re increases for Re > 100000.

Table 1 Simulated working conditions with different inlet velocities at a contraction angle of 3°

Group	Inlet velocity（m/s）	*Re*	Volume flow rate (m³/s)
1	0.1	4.322×10^3	0.031
2	0.2	8.643×10^3	0.062
3	0.5	2.161×10^4	0.156
4	1	4.322×10^4	0.312
5	2	8.644×10^4	0.623
6	5	2.161×10^5	1.559
7	10	4.322×10^5	3.117
8	15	6.483×10^5	4.676
9	20	8.644×10^5	6.234
10	28.49	1.229×10^6	8.881

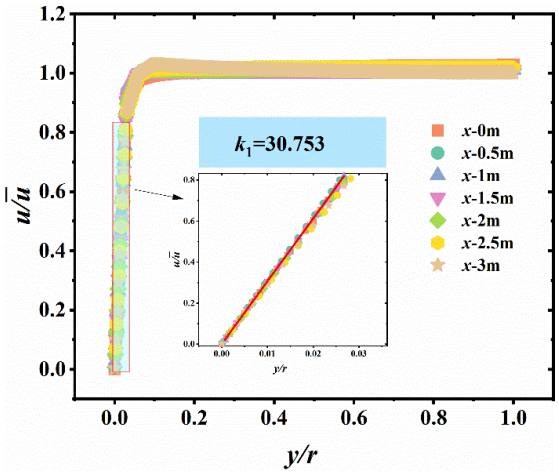

(a) u_0=0.1 m/s

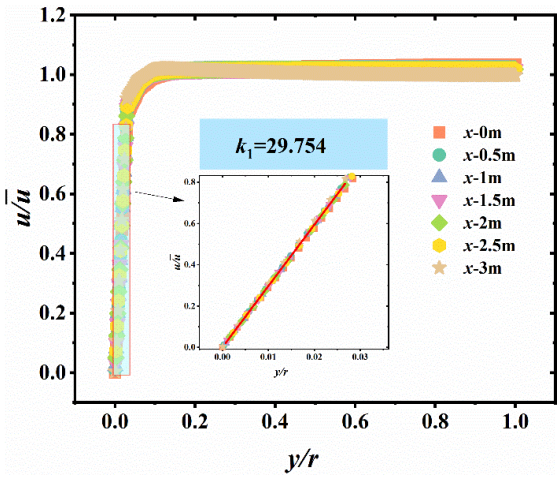

(b) u_0=20 m/s

Fig. 8 Velocity distribution of each section at different inlet velocities for a contraction angle of 3°. Only two sets of typical values are presented

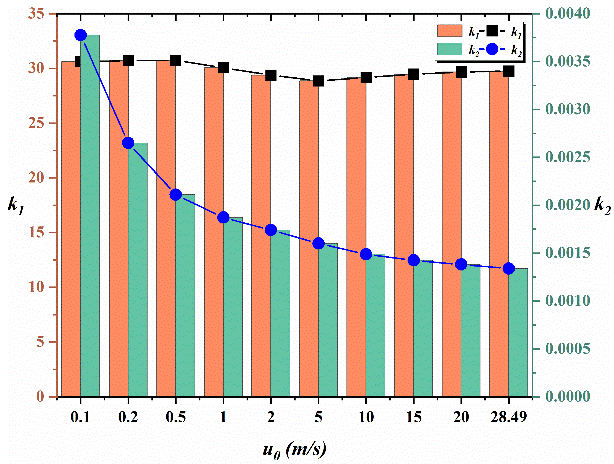

Fig. 9 Variation of k_1 and k_2 at different initial velocities

Next, a concise analysis of the total pressure loss at various Reynolds numbers and the proportion of pressure loss to the total inlet pressure is depicted in Fig. 10. The pressure loss increases with the inlet velocity and can be

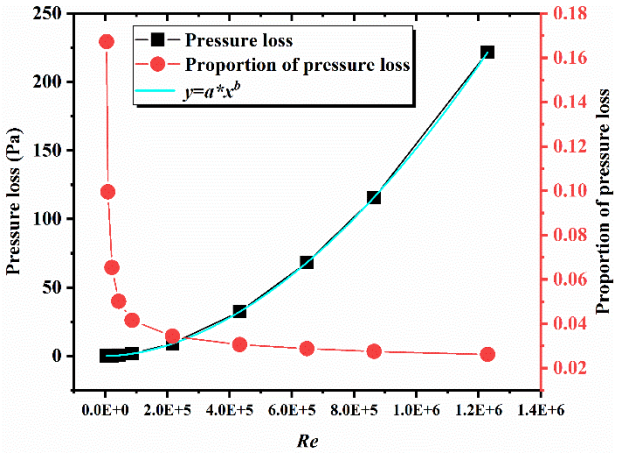

Fig. 10 Total pressure loss and proportion of pressure loss of the contraction pipe at different Reynolds numbers

determined by fitting the equation $\Delta P_t=1.326\times10^{-9}\cdot Re^{1.843}$. The coefficient of determination was approximately 1, indicating an excellent fit. The fitted formula was compared to the derived theoretical formula, and k_1 remained unaffected by the Reynolds number, whereas k_2 exhibited a negative correlation with *Re*. These results further support the accuracy of the theoretically derived Eq. (27).

The proportion of pressure loss was more significant at lower inlet velocities (u_0 < 2.3 m/s, i.e., *Re* < 100000) and decreased sharply as the inlet velocity increased. For higher inlet velocities (u_0 > 2.5 m/s), the proportion of pressure loss decreased slowly with an increasing inlet velocity and was below 4%.

4.3 Relationships between k_1, k_2, and the contraction angle

Similarly, employing the method of controlling variables by maintaining a constant inlet velocity (fixed at 20 m/s) and constant contraction pipe length (fixed at 3 m), the effect of varying the contraction angle on k_1/k_2 was studied. Table 2 lists the working conditions.

Figure 11 shows the fitted values of k_1 for various contraction angles. Four sets of typical values are presented. The calculation of k_2 was based on Eq. (27).

Table 2 Simulated working conditions with different contraction angles at an inlet velocity of u_0=20 m/s

Group	α (°)	tan(α□
1	1	0.01746
2	1.2	0.0209
3	1.5	0.0262
4	1.7	0.0297
5	2	0.0349
6	2.2	0.0384
7	2.5	0.0437
8	2.7	0.0472
9	3	0.0524
10	3.2	0.0559
11	3.5	0.0612
12	3.7	0.0647

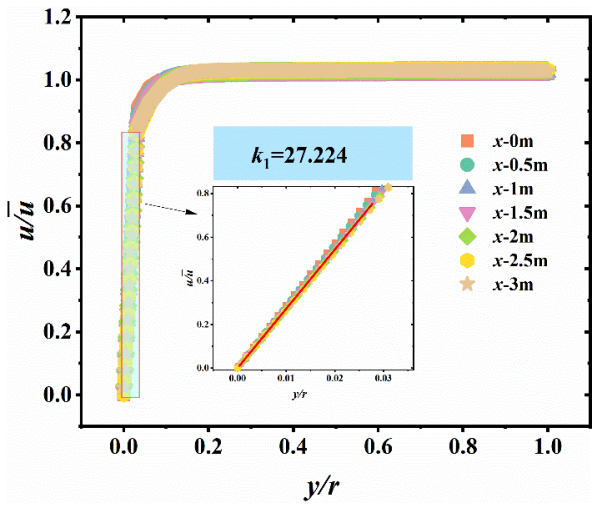

(a) α=1°.

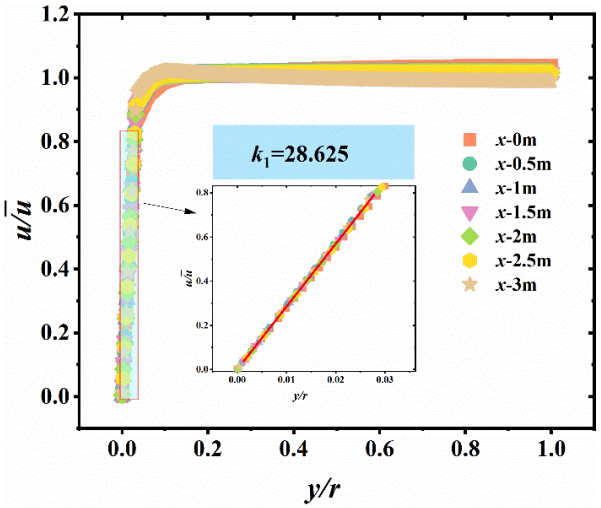

(b) α=3.7°.

Fig. 11 Velocity distribution of each section at different contraction angles with an inlet velocity u_0 of 20 m/s. Two sets of typical values are presented

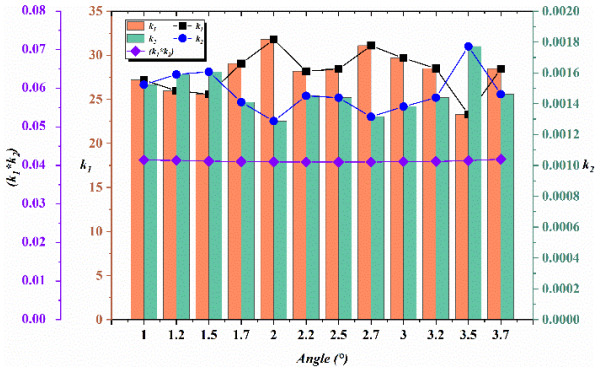

Fig. 12 Variation of $k_1/k_2/(k_1*k_2)$ versus the contraction angle

Figure 12 depicts the variations in k_1, k_2, and (k_1*k_2) with the contraction angle. Here, k_1, k_2, and the contraction angle are not entirely independent, as there exist some connections between them, as shown in Fig. 12. Specifically, k_1 and k_2 exhibit opposite changes, suggesting a reasonable relationship between $(k_1 \times k_2)$ and the contraction angle. Conversely, Fig. 12 demonstrates that (k_1*k_2) remained stable across different contraction angles, with a maximum change of only 1.2%. Hence, either k_1 or k_2 is related to the contraction angle, whereas (k_1*k_2) remains constant. Hence, (k_1*k_2) is independent of the contraction angle.

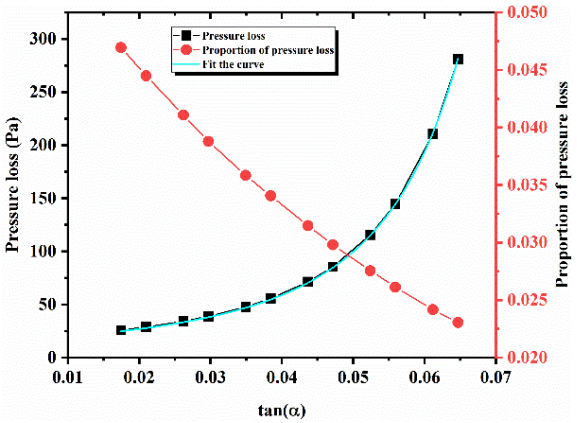

Fig. 13 Relationship between the pressure loss, proportion of pressure loss, and tangent values of different contraction angles

Figure 13 shows the pressure loss and proportion of the pressure loss in relation to the tangent value of the contraction angle. Equation (29) represents the fitting relationship for the pressure loss with a highly reliable coefficient of determination (R^2=0.99999), indicating the credibility of the fitting relationship. Equation (30) was derived by substituting each known condition into the pressure loss in Eq. (27), which was obtained via theory. The comparison of these two equations shows that (k_1*k_2) is independent of the angle and thereby provides further validation of the analysis mentioned above.

$$\Delta P_t = 0.36633 * \tan(\alpha)^{-1.03555}\left(\left(\frac{0.315}{0.315-3\tan(\alpha)}\right)^4 - 1\right) \quad (29)$$

$$\Delta P_t = \frac{\rho u_0^2 k_1^2 k_2^2}{2\tan(\alpha)}\left(\left(\frac{0.315}{0.315-3\tan(\alpha)}\right)^4 - 1\right) = \frac{245 k_1^2 k_2^2}{\tan(\alpha)}\left(\left(\frac{0.315}{0.315-3\tan(\alpha)}\right)^4 - 1\right) \quad (30)$$

5. DISCUSSION

Section 4 discussed the relationships between k_1, k_2, the Reynolds number, and the contraction angle. In general, (k_1*k_2) is related to the Reynolds number but not to the contraction angle. Therefore, determining its relationship with the Reynolds number can simplify the pressure loss model for a smooth gradual contraction pipe. Figure 14(a) shows a scatter plot of $(k_1*k_2)^2$ versus the Reynolds number. By fitting, the equation $(k_1*k_2)^2=0.0148\cdot(Re)^{-0.157}$ was obtained with a goodness-of-fit value of 0.87. Substituting this into Eq. (28) yields a general expression for the local loss coefficient of a

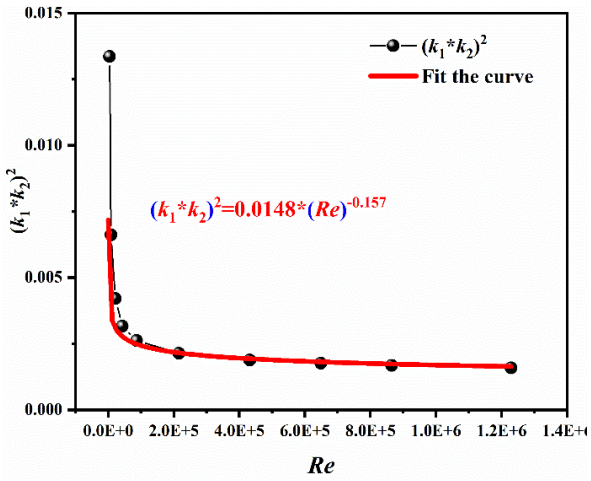

(a)

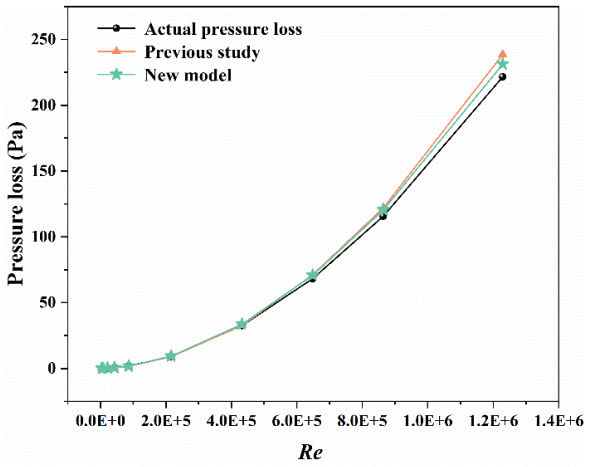

(b)

Fig. 14 (a) Relationship between $(k_1*k_2)^2$ and *Re*. (b) Comparison between the results of a previous study and those of the proposed model at different *Re* values

gradually contracting pipe (Eq. (31)). This coefficient is applicable in the range of $4000 < \mathrm{Re} < 10^6$.

$$\xi_{\max} = \frac{k_1^2 k_2^2}{\tan\alpha}\left(\frac{S_0^2}{S_x^2}-1\right) = \frac{0.0148}{\mathrm{Re}^{0.157}\tan\alpha}\left(\frac{S_0^2}{S_x^2}-1\right)$$

$$\xi_{\min} = \frac{k_1^2 k_2^2}{\tan\alpha}\left(1-\frac{S_x^2}{S_0^2}\right) = \frac{0.0148}{\mathrm{Re}^{0.157}\tan\alpha}\left(1-\frac{S_x^2}{S_0^2}\right) \quad (31)$$

Here, we state the limitations regarding the scope of applicability of this model. The application of this model in situations beyond this range are likely to result in significant errors. These limitations include the limitations relating to the Reynolds number, which primarily consider the substantial impact of roughness at lower Reynolds numbers, as well as those relating to the influence of fluid compressibility at higher Reynolds numbers. However, large contraction angles can lead to an increase in the Reynolds number, and fluid compressibility has an impact. These are directions that future research must consider.

Figure 14(b) illustrates a comparative analysis between an existing model developed by other researchers and the novel model proposed in this study, specifically focusing on the prediction of the actual pressure loss within the simulation. Both models exhibited a high level of accuracy; however, the proposed model demonstrated a marginally higher degree of precision. Notably, as the Reynolds number increases, the absolute error associated with the previous model tends to increase, which underscores the broader applicability of our model.

Furthermore, the application of the previous model necessitates a preliminary calculation of the Darcy friction factor, which is feasible through reference to the Moody chart in engineering practice and substantially amplifies the computational overhead. In contrast, the local loss coefficient model established in this study offers distinct advantages. These results enhance the precision of predicting local pressure losses in gradually tapered pipes, streamlines the computational procedure, and allows the determination of local loss factors based solely on the Reynolds number to thereby facilitate the more efficient calculation of pressure losses. This advancement is of significant value in the context of engineering practice because it offers a practical and efficient method for assessing local losses in pipe systems.

6. CONCLUSIONS

In this study, we developed a semi-empirical model for predicting the pressure loss in smooth contraction pipes. The proposed model is valid within the Reynolds number range of 4000–1,000,000. The model, which is based on a variant of Stokes' formula, accurately predicts the total pressure loss, pressure gradient, and local loss coefficient with improved accuracy, compared with existing empirical formulas. The model not only facilitates the stress analysis of contraction pipes but also enables the rapid calculation of local pipe resistance when only the flow rate is known, thereby significantly reducing measurement and time costs. These results are important for the determination of local losses in engineering practice, particularly for fan pipes with gradually contracting structures.

The potential to expand the applicability of this model to a broader range of conditions and geometries presents a promising avenue for future research. The integration of our model with CFD simulations allows for more complex flow scenarios and further enhances the precision of modeling complex fluid systems.

In addition, exploring the applicability of the model to various pipe materials and geometries could broaden its use in optimizing fluid flow systems across different industries. This study provides a foundation for future advancements in fluid mechanics research and the development of more efficient fluid-based applications.

ACKNOWLEDGMENTS

This study was supported by the Students' Innovation and Entrepreneurship Foundation of USTC

(CY2023G021) and the National Natural Science Foundation of China (52404260).

CONFLICTS OF INTEREST

The authors declare that they have no competing financial interests or personal relationships that may have influenced the work reported in this study.

AUTHOR CONTRIBUTIONS

Huazhong Sun: Methodology; Formal analysis; Writing - Original draft; **Xiaolong Zhu:** Writing - Review & editing; Supervision; **Xishi Wang:** Writing - Review & editing; Project administration; Funding acquisition; **Jiangyue Zhao:** Data Curation; **Shi Hu:** Visualization; Jialing Yu: Software.

REFERENCES

Abou-Kassem, A. J., Bizhani, M., & Kuru, E. (2023). A review of methods used for rheological characterization of yield-power-law (YPL) fluids and their impact on the assessment of frictional pressure loss in pipe flow. *Geoenergy Science and Engineering*, *229*, 212050. https://doi.org/10.1016/j.geoen.2023.212050

Ayas, M., Skocilas, J., & Jirout, T. (2021). Friction factor of shear thinning fluids in non-circular ducts – a simplified approach for rapid engineering calculation. *Chemical Engineering Communications*, *208*(8), 1209-1217. https://doi.org/10.1080/00986445.2020.1770232

Badekas, D., & Knight, D. D. (1992). Eddy correlations for laminar axisymmetric sudden expansion flows. *Journal of Fluids Engineering*, *114*, 119-121. https://doi.org/10.1115/1.2909986

Bae, Y. M., & Kim, Y. I. (2014a). Prediction of local loss coefficient for turbulent flow in axisymmetric sudden expansions with a chamfer: Effect of Reynolds number. *Annals of Nuclear Energy*, *73*, 33-38. https://doi.org/10.1016/j.anucene.2014.06.032

Bae, Y. M., & Kim, Y. I. (2014b). Prediction of local pressure drop for turbulent flow in axisymmetric sudden expansions with chamfered edge. *Chemical Engineering Research and Design*, *92*, 229-239. https://doi.org/10.1016/j.cherd.2013.07.016

Brown, G. O. (2002). The history of the Darcy-Weisbach equation for pipe flow resistance. *Environmental and Water Resources History*, 34-43. http://dx.doi.org/10.1061/40650(2003)4

Bullen, P., Cheeseman, D., & Hussain, L. (1988). The effects of inlet sharpness on the pipe contraction pressure loss coefficient. *International Journal of Heat and Fluid Flow*, *9*(4), 431-433. https://doi.org/10.1016/0142-727X(88)90012-4

Daugherty, R. L., Franzini, J. B., & Finnemore, E. J. (1985). *Fluid mechanics with engineering applications*. Eighth edition.

FLUENT Inc. (2019). *FLUENT User's Guide*.

Gosteev, Y. A., Obukhovskiy, A. D., & Salenko, S. D. (2018). *On head losses in conical diffusers*. AIP Conference Proceedings. https://doi.org/10.1063/1.5065142

Hooper, W. B. (1981). The two-K method predicts head losses in pipe fittings. *Chemical Engineering*, *88*, 96-100.

Hooper, W. B. (1988). Calculate head loss caused by change in pipe size, *Chemical Engineering*, *95*, 89–92.

Iguchi, M., & Ohmi, M. (1986). Loss coefficients for flows through a sudden expansion and a sudden contraction closely placed. *Transactions of the Japan Society of Mechanical Engineers Series B*, *52*(481), 3252-3258. https://doi.org/10.1299/kikaib. 52.3252

Kao, Y. H., Jiang, Z. W., & Fang, S. C. (2017). A computational simulation study of fluid mechanics of low-speed wind tunnel contractions. *Fluids*, *2*(23), 23. https://doi.org/10.3390/fluids2020023

Launder, B. E., & Spalding, D. B. (1972). *Lectures in Mathematical Models of Turbulence*. Academic Press.

Liu, X., Li, D., Qi, P., Qiao, W., Shang, Y., & Jiao, Z. (2023). A local resistance coefficient model of aircraft hydraulics bent pipe using laser powder bed fusion additive manufacturing. *Experimental Thermal and Fluid Science*, *147*, 110961. https://doi.org/10.1016/j.expthermflusci.2023.110961

Liu, X., Liu, J., Wang, D., & Zhao, L. (2021). Experimental and numerical simulation investigations of an axial flow fan performance in high-altitude environments. *Energy*, *234*, 121281. https://doi.org/10.1016/j.energy.2021.121281

Nikuradse, J. (1933). Flow laws in raised tubes. *Zeitschrift Des Vereines Deutscher Ingenieure*, *77*, 1075-1076.

Oliveira, P. J., Pinho, F. T., & Schulte, A. (1998). A general correlation for the local loss coefficient in Newtonian axisymmetric sudden expansions. *International Journal of Heat and Fluid Flow*, *19*, 655-660. https://doi.org/10.1016/S0142-727X(98)10037-1

Pak, B., Cho, Y. I., & Choi, S. U. S. (1990). Separation and reattachment of non-Newtonian fluid flows in a sudden expansion pipe. *Journal of Non-Newtonian Fluid Mechanics*, *37*, 175-199. https://doi.org/10.1016/0377-0257(90)90004-U.

Rennels, D. C. (2022). *Pipe flow: A practical and comprehensive guide*. Second edition. Hoboken, NJ: Wiley. Part 2, Loss coefficients; Chapter 10, Contractions (pp. 113-125). https://lccn.loc.gov/2021049297 (LC ebook record)."

Scott, P., Mirza, F., & Vlachopoulos, J. (1986). A finite element analysis of laminar flows through planar and axisymmetric abrupt expansions. *Computers & Fluids*, *14*, 423-432. https://doi.org/10.1016/0045-7930(86)90016-2

Shames, I. H. (1992). *Mechanics of fluids*. McGraw-Hill, New York.

Shih, T. H., Liou, W. W., Shabbir, A., Yang, Z. G., & Zhu, J. (1995). A new k-ε eddy viscosity model for high Reynolds number turbulent flows. *Computers & Fluids*, *24*(3), 227-238. https://doi.org/10.1016/0045-7930(94)00032-T

Sobieski, W. (2024). Estimation methodology of pressure losses in non-circular pipes. *Journal of Applied Fluid Mechanics*, *17*(7), 1368-1378. https://doi.org/10.47176/jafm.17.7.2518

Štigler, J. (2014). Analytical velocity profile in tube for laminar and turbulent flow. *Engineering Mechanics*, *21*(6), 371-379. https://doi.org/10.13140/2.1.3153.5046

Wilcox, D. C. (1994). *Turbulence Modeling for CFD*. DCW Industries, Inc.

Wu, H., Wang, Y., & Liu, Y. (2024). Flow characteristics and resistance coefficients of local components of building heat-moisture-oxygen transport pipelines in the Tibetan Plateau. *Journal of Building Engineering*, *91*, 109532. https://doi.org/10.1016/j.jobe.2024.109532

Xu, J., Yao, Y., Yan, H., Zhou, N., Su, H., Li, M., Liu, S., & Wang, H. (2024). Experimental study of pipeline pressure loss laws with large-size gangue slurry during the process of industrial-grade annular pipe transportation. *Construction and Building Materials*, *436*, 136993. https://doi.org/10.1016/j.conbuildmat.2024.136993

Yan, B. H., & Gu, H. (2013). Effect of rolling motion on the expansion and contraction loss coefficients. *Annals of Nuclear Energy*, *53*, 259-266. https://doi.org/10.1016/j.anucene.2012.09.019

Yan, B., Gu, H., & Lei, Y. (2012). CFD analysis of the loss coefficient for a 90° bend in rolling motion. *Progress in Nuclear Energy*, *56*, 1-6. https://doi.org/10.1016/j.pnucene.2011.11.006

Yao, L. M., Liu, J. B., Li, X. Y., Yue, Q. B., Liu, Y. X., & Wang, H. T. (2019). Application of the building block approach to characterize the pressure loss of water and fracturing fluid in contraction-expansion pipe. *Journal of Petroleum Science and Engineering*, *176*, 51-61. https://doi.org/10.1016/j.petrol.2018.12.010

Yogaraja, L., Liyanagamage, N., & De Silva, K. (2021). *Comparison of experimental results with empirical relationships for energy losses in pipe flow*. 2021 Moratuwa Engineering Research Conference (MERCon) (pp. 522-527). Moratuwa, Sri Lanka. https://doi.org/10.1109/MERCon52712.2021.9525661